Volume 22, No 2 | International Journal of Radiation Research, April 2026

Applying the deep learning method for dose estimation in radiotherapy

N. Mahdavi[1], M. Shamsaei Zafarghandi[1*], S. Setayeshi[1], H.A. Nedaie[2]

[1]*Department of Physics and Energy Engineering, Amir Kabir University of Technology, Tehran, Iran*
[2]*Radiation Oncology Research Centre, Cancer Institute, Tehran University of Medical Sciences, Tehran, Iran*

► ***Original article***

Corresponding author:
M. Shamsaei Zafarghandi, Ph.D.,
E-mail: *pysham@aut.ac.ir*

Received: January 2024
Final revised: November 2024
Accepted: January 2025

Int. J. Radiat. Res., April 2026; 24(2): 501-508

DOI: 10.61186/ijrr.24.2.29

Keywords: *Dose prediction, deep Learning, U-net architecture, inhomogeneity, radiotherapy.*

ABSTRACT

Background: The present study's main objective is to develop the model based on the U-net architecture to estimate dose distribution in heterogeneous phantoms by applying water phantom dose distribution and the characteristics of a heterogeneous phantom. ***Materials and Methods:*** The proposed model was developed based on the U-Net architecture, which includes five input channels and one output channel with dimensions 32×32×64 in the associated x, y, and z directions. Two hundred heterogeneous phantoms with water, lung, and bone materials at various depths were simulated using the Dosxyznrc code. Subsequently, the external photon source was applied to irradiate all the heterogeneous phantoms. The dose distribution of the water phantom served as the initial input channel, along with other input channels containing physical components of the heterogeneous phantoms. The dose distributions calculated by the Dosxyznrc code for each heterogeneous phantom were used as output. The developed model was trained using all the provided input and output data associated with the training data on the Google Colab execution platform. ***Results:*** The findings show that over 98% of total voxels met the 3%/3 mm gamma test requirements in the water area before heterogeneity. Furthermore, more than 99% of the voxels in the heterogeneous lung and bone medium satisfied the gamma test requirement of 3%/3 mm. ***Conclusion:*** The dose distribution in heterogeneous phantoms can be predicted quickly and accurately using the developed model based on a U-net architecture, which leverages the distribution of dose in a water phantom and the physical properties of the heterogeneous phantom.

INTRODUCTION

The effectiveness of radiation therapy treatment and its adverse effects are significantly influenced by the radiation dose received by the tumor and nearby normal tissues [1, 2]. Accurate and efficient dose calculation in radiotherapy can serve as a predictor and reliable model for the relationship between dose distribution and clinical outcomes, ultimately improving future treatment [1, 2]. Over the years, dose calculation algorithms in treatment planning systems (TPSs) have evolved over several generations.

The initial iteration of an algorithm, based on physics principles, is a correction-based approach [3]. However, its accuracy decreases in heterogeneous mediums due to the loss of electronic equilibrium [4-7]. Subsequently, model-based approaches were developed to account for the physics of heterogeneous mediums [8, 9]. The third type of dose algorithm is the Monte Carlo algorithm, which uses exact physics principles and measurable data or recognized formulas to simulate energy transfer and deposition of each particle (photons, electrons, etc.) [9-11]. However, the Monte Carlo technique simulates the movement of each particle separately, resulting in longer calculation times and requiring a powerful computer.

In recent years, deterministic radiation transport techniques have been developed and widely used in clinical settings. One such technique is the Acuros® XB Advanced Dose Calculation, a member of the Linear Boltzmann Transport Equation Solvers, which offers competitive dosimetric accuracy compared to its Monte Carlo counterpart, with the added benefit of significantly better computational efficiency [10, 12]. Additionally, deep neural networks, known as deep learning, have been applied in various scientific fields [13-15]. In radiation therapy, machine learning and deep learning (DL), including convolutional networks, have been used for treatment planning [16, 17]. The knowledge-based planning paradigm, which has been the focus of much research on dose prediction in radiotherapy, uses data from previous patient plans to predict a patient's dose volume histogram (DVH) and dose constraints [18-22].

While KBP has seen significant advancements, it requires a considerable amount of time and effort to select handicraft elements, such as spatial data on organs at risk (OAR) and planning target volumes (PTV) [19, 22-24]. Furthermore, it is limited by the inherent information present in the data [19]. Another challenge in dose prediction using deep learning

[DOI: 10.61186/ijrr.24.2.29]

methods is the loss of spatial consistency regarding neighboring anatomy, which can exhibit significant differences in CT numbers and steep gradients of tissue heterogeneity. In this study, we have developed a deep learning model based on the U-Net architecture to predict dose distribution in heterogeneous phantoms. Our model incorporated influence parameters related to heterogeneous environments and the radiation field to forecast dose distribution. The primary objective was to create a deep learning-based model that can predict dose distribution more rapidly than the Monte Carlo approach while maintaining comparable accuracy.

MATERIALS AND METHODS

Design Network architecture

The standard two-dimensional U-Net architecture was expanded to the three-dimensional U-Net architecture to anticipate dose distribution in a heterogeneous phantom [25, 26]. The network expected five input channels and one output channel. Each input and output channel consisted of a 3D volume with dimensions of 32×32×64 in the associated x, y, and z directions. The designed network comprised five hierarchical layers. The encoding path at each hierarchy level included consecutive layers of two convolutions operation with a kernel size of (3×3×3). Furthermore, rectified linear units were used as an activation function next to each convolution operation [27]. Between each pair of sequential hierarchy layers, a max-pooling operation was used with a kernel size of (2×2×2) and a voxel stride of two to gradually diminish the size of the feature maps from (32×32×64) to (2×2×4). In the decoding path, each layer included an up-convolution of (2×2×2) with strides of two in each direction, followed by two convolution operations with a kernel size of (3×3×3). Additionally, rectified linear units came after each convolution operation.

Dropout was also used at each convolutional layer to minimize overfitting [28]. The final layer also included a (1×1×1) convolution followed by a linear activation function, resulting in an original output channel representing the predicted dose. A schematic of the designed U-Net architecture is illustrated in figure 1. The number of concatenated features is revealed below the boxes, and the size of the three-dimensional feature maps is indicated next to the boxes.

Heterogeneous phantoms simulation and dataset generation

In this study, we simulated two hundred heterogeneous phantoms of voxels filled with specific materials like water, lung, and bone at different depths using the Dosxyznrc code [20]. All heterogeneous phantoms had the same geometry, with dimensions of 8×8×16 cm and consisting of 32×32×64 voxels in the associated x, y, and z directions. The water, lung, and bone materials with densities of ρ=1000 kg/m^3, ρ=260 kg/m^3, and ρ=1850 kg/m^3 were used in a heterogeneous phantom.

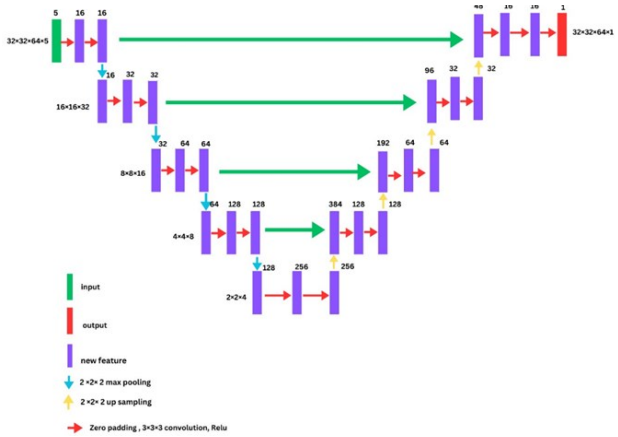

Figure 1. Illustration of the designed U-Net architecture used to develop the dose prediction model. The designed U-Net architecture accepts five input channels, each with dimensions of 32×32×64, and to produce an output channel with the exact dimensions in the x, y, and z directions. The encoding path at each hierarchical level included consecutive layers of two convolution operations, each with a kernel size of 3×3×3.

The parallel square radiation field with dimensions of 5 cm × 5 cm from eleven types of sources, as explained in the Dosexyznrc code, was simulated [20]. Furthermore, the 6 MV photon beam spectrum, called the Mohan spectrum, from the EGS4 Spectra Library was chosen as the primary source in the simulations [29].

The Simorgh supercomputer at Amir Kabir University was utilized to calculate dose distribution in a heterogeneous phantom. Each calculation was executed with 1.6E9 histories to achieve an overall statistical uncertainty below 0.3%, and each simulation lasted approximately ten hours.

The dose distributions for two hundred phantoms were extracted from the output files generated by the Dosxyznrc code. Each output was multiplied by 1e15 to represent all monitor units applied to the accelerator. The final output for each heterogeneous phantom was used to build matrices with dimensions of (32×32×64) in the x, y, and z directions. According to the objective of this study, five input channels were designed for the U-Net architecture. The water phantom's dose distribution served as the initial input channel. The other input channels were selected based on physical factors influencing dose computation in a heterogeneous medium. The photon energy deposited in tissue contains a two-step procedure. In the first walk, photons interact with the tissue to transfer kinetic energy to charged particles (TERMA). Subsequently, the charged particles deliver their energy through ionization and excitation reactions along a limited track.

[DOI: 10.61186/ijrr.24.2.29]

In a heterogeneous phantom, TERMA is obtained by multiplying the total mass attenuation by the energy fluence (ψ) at a point r (x, y, z) [30]. The energy fluence (ψ) is determined by the inverse of each voxel's distance from the central reference point of the radiation field. Therefore, the second input channel was chosen as the matrix representing each voxel's distance from the reference point at the center of the radiation field [30]. Additionally, the matrix of the mass density of heterogeneous phantoms was used as an input for the network because of the impact of each voxel's mass density on calculating the TERMA in heterogeneous phantoms [30, 31].

For the inhomogeneity correction, the CT numbers of every voxel in the heterogeneous phantom were taken as input data. Consequently, the U-net architecture's fourth input was the matrix containing the heterogeneous phantoms' CT numbers [30].

The primary dose and scattered dose components include the two parts of the integrated dose in the phantom. The primary particle is responsible for the primary dose, while the secondary particle is responsible for the scattered dose. The voxels directly under the primary radiation's path were assigned number 1, whereas the remaining voxels received zero. Therefore, the fifth input for the U-net architecture is a matrix consisting of zero or one value representing the simulated radiation field. All matrices for input and output channels have dimensions (32×32×64) in the associated x, y, and z directions [30].

Training

The Google Colab execution platform, using Keras libraries, was utilized to execute the designed U-net architecture with all the provided inputs and outputs [32]. Google Colaboratory, or Google Colab, is a cloud-placed machine learning platform. It gives a Jupyter notebook with a Python programming environment and includes libraries such as TensorFlow and Keras for machine learning projects. The Google Colab utility offers 358.27 GB of hard disk space and 12.72 GB of RAM in one runtime [33, 34]. Two hundred heterogeneous phantom data were randomly divided into three groups: training, validation, and testing data, utilizing the train_test_split function in Python. Finally, one hundred and twenty data were applied for training, sixty for validation, and twenty for testing in the designed model. The developed model took inputs in the form of a five-channel matrix with dimensions of (32×32×64), and the output is in the form of a single-channel matrix with dimensions of (32×32×64). Also, the mean squared error (MSE) was used as the loss function.

The ADAM algorithm is a valuable stochastic gradient method for problems with extensive data or parameters [35]. The ADAM optimizer from the Keras library was selected to improve the Deep Learning training process. It used learning rate, beta1, and beta2 as variable input values with numerical values 1E-4, 0.9, and 0.999, respectively [35]. Early stopping was utilized as a regularization technique to avoid overfitting. Additionally, the iteration with the best model weights was opted based on the validation loss, a well-known method to prevent overfitting the model to the data [36, 37].

Statistical data analysis

The deviation (D), as equation (1), was applied to compare the dose distribution predicted by the developed model with the dose distribution calculated using Monte Carlo simulation as the reference data. Also, D_z represents the reference dose at a depth of Z, and $D_{z(U\text{-}net)}$ represents the dose predicted by the developed model at a depth of Z.

$$D(\%) = 100 * \frac{\left(D_{z(U-net)} - D_{z,MC}\right)}{D_{z,MC}} \quad (1)$$

Additionally, the 2D dose distribution predicted using the developed model was examined with the dose distribution obtained by the Monte Carlo approach employing the gamma analysis developed by Low *et al*., as outlined in equations 2 and 3 [38].

$$\gamma(r_r) = \min\{\Gamma(r_e, r_r)\}\forall(r_{de}) \quad (2)$$

$$\Gamma_r(r_e, r_r) = \sqrt{\frac{(r_e - r_r)^2}{\Delta d^2} + \frac{(D_e - D_r)^2}{\Delta D^2}} \quad (3)$$

In equations 2 and 3, r_r represents the reference position, and r_e represents the position of the comparison point. The D_r represents the voxel dose value calculated using the Monte Carlo method, while D_e represents the dose predicted by the developed model. Gamma analysis (10) was performed, applying different threshold criteria: distance to agreement DTA = 1 mm, 2 mm, and 1 mm, dose difference ΔD of 1%, 2%, and 3%. Every computation used global gamma indices, with the ΔD normalized to the global maximum dose of heterogeneous phantoms [38].

The criteria of 3%/3 mm recommended by Low *et al*. and the AAPM task group (TG-119) were applied as the main criteria to compare the results of the designed model and the Monte Carlo method [38, 39]. Additionally, when using the requirements of 3%/3mm, the gamma pass rate of more than 95% at the evaluated point was approved according to the suggestion by the AAPM Task Group(TG-119) [39, 40]. Moreover, the t-test was used as the statistical test to calculate the p-value, assuming the null hypothesis was confirmed.

RESULTS

The developed model predicted the percentage

[DOI: 10.61186/ijrr.24.2.29]

depth dose and axial dose profiles for the heterogeneous phantoms, which were part of the testing data. The expected dose distribution was compared to the ground-truth target dose measured using the Dosexyznrc Monte Carlo code.

PDD and relative dose profile for first heterogeneous phantom

The first heterogeneous phantom used to study PDDs and 2D dose maps is depicted in figure 2. The percentage depth dose (PDD) curves, calculated by the developed model and measured using Monte Carlo simulation, are displayed in figure 3A. The difference between the PDD curves is also illustrated in figure (3A) with a red bar.

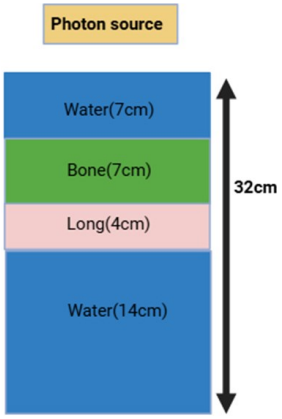

Figure 2. The heterogeneous phantom, which contains several distinct regions for evaluating dose distribution. The first layer consists of water, with a thickness of 7 cm, and the second layer consists of bone, also 7 cm thick. The third layer is the lung, with a thickness of 4 cm, and the fourth layer is water, with a thickness of 14 cm.

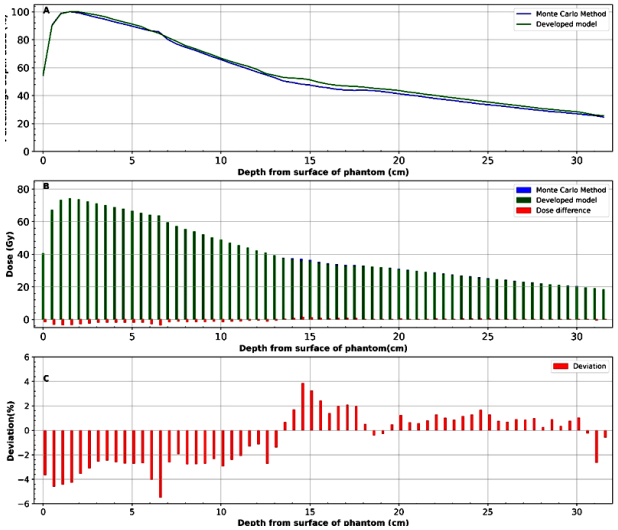

Figure 3. Illustration the dose distribution along the center of the heterogeneous phantom. **(a)** Percent Dose Depth (PDD) curves were generated using Monte Carlo simulations and predicted by the developed model. **(b)** The actual values of the dose distribution were obtained using both methods, along with the differences in dose distribution values. **(c)** The dose deviation was determined using the Monte Carlo simulation and predicted by the developed model.

Figure 3B displays a bar chart comparing the dose values calculated using the Monte Carlo method with those predicted by the designed model for all voxels along the central beam axis direction. The differences in dose value between the Monte Carlo method and the developed model are illustrated with red bars in figure 3B. Also, figure 3C displays the dose deviation in percentage calculated using equation (1) on the bar chart. In this heterogeneous phantom, the maximum dose was estimated to be 73.9 Gy using the Monte Carlo method, while the designed model predicted the maximum dose to be 71.1 Gy. Therefore, the deviation of the maximum dose values when applying the two methods was 3.7%. In addition, for all voxels along the centrality direction, the p-value for data obtained from the two methods has been calculated to be more than 0.85.

Figures 4A and 4B display the two-dimensional (x, z) images of the dose distribution and isodose curves for the Monte Carlo method and the developed model, respectively. Also, the difference between dose distribution measured by the Monte Carlo method and the developed model is illustrated in figure 4C. Isodose curves for values of 80%, 70%, 60%, 50%, and 30% of the maximum dose measured using the Monte Carlo method are depicted in figure 4. Also, figure 4D displays the isodose contours for the dose distribution measured using the Monte Carlo method and the dose distribution predicted by the developed model.

The results of isodose curves show good matching in the water area before heterogeneities and in the bone area. Additionally, a relatively small difference in the isodose curves was seen in the part of the lung. Also, the p-value was calculated with an accuracy of over 0.94 for dose distribution data measured by the Monte Carlo method and predicted by the developed model in the Z and X directions.

Figure 5 shows dose profiles for the first heterogeneous phantom at different depths calculated by the Monte Carlo method and predicted by the developed model. Figure 5A shows dose profiles in the homogeneous water area at a depth of 5 cm from the phantom surface, while figure 5B depicts dose profiles in the bone heterogeneous medium at a depth of 10 cm from the phantom. Figure 5C shows dose profiles at the interface between the bone and lung layers at a depth of 14 cm. Also, figure 5C illustrates that the predicted dose distribution aligns well with the dose distribution calculated by the Monte Carlo method at the interface between bone and lung environments, despite the lack of electron equilibrium due to the transition from the heterogeneous bone area to the lung environment. Additionally, figure 5D shows a slight difference in dose profiles obtained using two methods at a depth of 16.5 cm in the heterogeneous lung layer within the radiation field. Finally, figure 5E shows dose profiles at the interface between the lung and the fourth water layer at a depth of 18 cm. Also, figure 5F illustrates dose profiles in the fourth water layer at a depth of 25 cm of the heterogeneous phantom.

The gamma values of each voxel in the two-dimensional planes (x, y) at various depths were

[DOI: 10.61186/ijrr.24.2.29]

computed for the initial heterogeneous phantom. Table 1 lists and summarizes the percentages of voxels where the gamma values were less than one. Also, p-values for dose distribution calculated using Monte Carlo and predicted by the developed model at specific depths in the heterogeneous phantom, as illustrated in figure 5, were measured and specified in table 1.

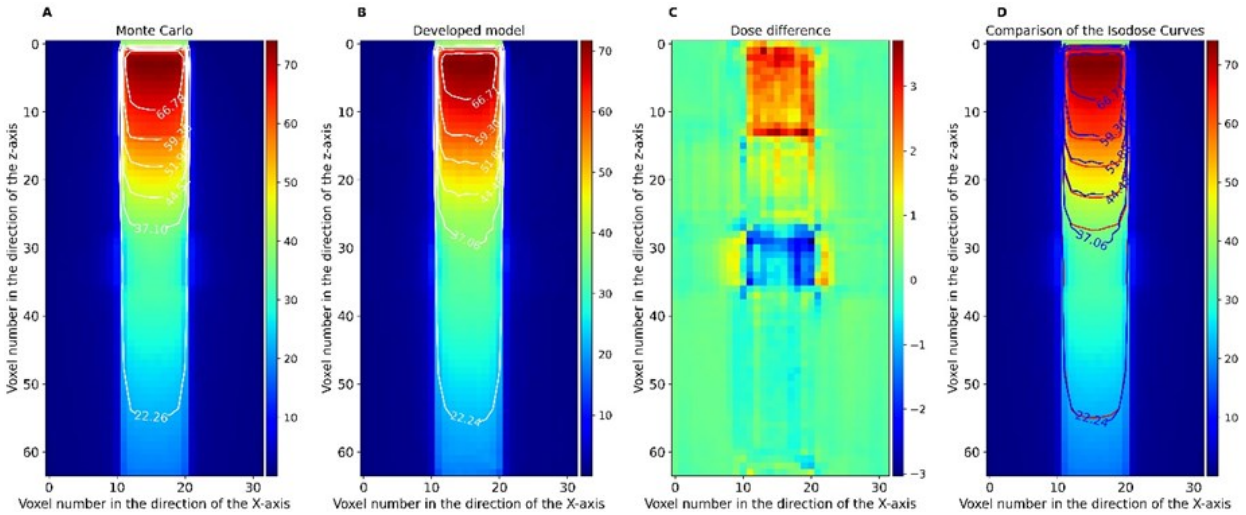

Figure 4. Illustration of the two-dimensional (x, z) images of the dose distribution and isodose curves. **(A)** The dose distribution and isodose curves are calculated using the Monte Carlo method. **(B)** The dose distribution and isodose curves are predicted using the developed model. **(C)** The difference between the dose distribution calculated by the Monte Carlo method and that predicted by the developed model. **(D)** A comparison of the isodose curves for values of 80%, 70%, 60%, 50%, and 30% of the maximum dose obtained from both methods.

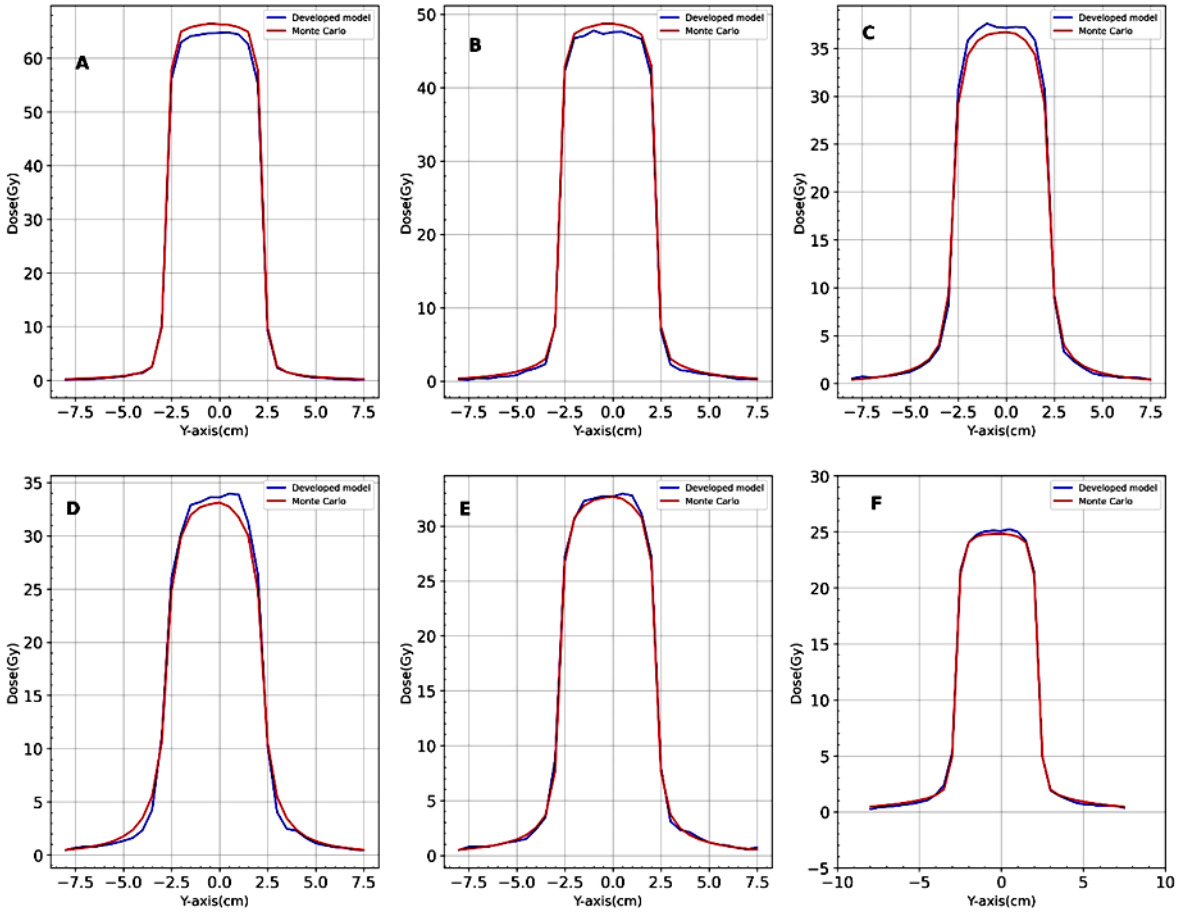

Figure 5. Illustration the dose profiles in the heterogeneous phantom at various depths from the surface of the phantom. **(A)** the dose profiles in the water medium at a depth of 5 cm from the surface of the phantom. **(B)** the dose profiles in the bone heterogeneous region at a depth of 10 cm. **(C)** the dose profiles at the interface between the bone and lung layers at a depth of 14 cm. **(D)** the dose profiles at a depth of 16.5 cm within the heterogeneous lung layer. **(E)** The dose profiles at the interface between the lung and the fourth water layer at a depth of 18 cm. **(F)** Finally, the dose profiles in the fourth water layer at a depth of 25 cm.

[DOI: 10.61186/ijrr.24.2.29]

Table 1. Presentation the gamma passing rate results and the P-value for the for-dose distribution predicted by the developed model as predicted dose and calculated dose distribution by Monte Carlo simulation as reference dose for several depths in the heterogeneous phantom.

first heterogeneous phantom	gamma passing rate				P-value
	Depth (cm)	$\gamma_{1\%}$	$\gamma_{2\%}$	$\gamma_{3\%}$	
In the water medium before heterogeneity	5	90.3	91.4	98.3	0.93
Interface of water and bone	7	90.6	94.8	98.8	0.95
Within the bone heterogeneity	10	91.1	98.9	99.9	0.93
Interface of bone and lung	14	88.2	94.2	99.2	0.95
Within the lung heterogeneity	16.5	86.2	95.4	99.3	0.98
Interface of lung and water	18	95.8	99.9	95.8	0.97
In the water medium Beneath the heterogeneity	25	100	100	100	0.99

DISCUSSION

According to the recommendations of Task Group 53, several methods can be used to compare predicted dose distributions with reference dose distributions [41]. One of these methods involves comparing depth doses and beam profiles between the predicted and reference doses. Given this, figure 3A illustrates the agreement between the percentage depth dose (PDD) curves predicted by the developed model and those observed using the Monte Carlo method, showing a discrepancy of less than 2%. Additionally, the bar graph in figure 2B indicates that the numerical values representing the differences in dose distribution obtained by both methods for the heterogeneous region decrease after passing through the build-up area. Furthermore, figure 3C shows that the deviation typically remains between ±4% and decreases in the water environment after passing through heterogeneous layers.

Another suggestion from Task Group 53 was to compare isodose curves and create a graphical display of dose differences by subtracting the reference and predicted dose distributions [41]. As seen in figures 4A, 4B, and 4D, the results of the isodose curves for values of 80%, 70%, 60%, 50%, and 30% of the maximum dose show good agreement with the isodose curves in the heterogeneous phantom. Additionally, the graphical representation of dose differences in figure 4C illustrates minimum dose variation. The computed p-value for the dose distribution related to figures 4A and 4B indicates no significant difference between the two methods, with a probability exceeding 0.94.

According to figure 5, the cross-sectional profiles of the dose distribution obtained from the developed model exhibit the exact symmetry as those obtained from the Monte Carlo method in various regions of the heterogeneous phantom, including bone, lung, and the interfaces between these inhomogeneous areas. The results related to p-values in table 1, corresponding to specific depths in figure 5, suggest that the dose distributions produced by the developed model with p-values more than 90% closely resemble the dose distribution measured by the Monte Carlo method.

Furthermore, the gamma passing rate results in table 1 show that more than 98% of voxels pass the gamma test with criteria of 3%–3 mm in water areas before encountering heterogeneity. In addition, all voxels in the last layer of water in the heterogeneous phantom pass the gamma test with criteria of 1%/1 mm. These results indicate that the dose distribution is accurately predicted for the final layer of water, regardless of the impact of the preceding heterogeneous layers. For inhomogeneities such as bone, over 99.1% of voxels pass the gamma test with criteria of 3%/3 mm, and for lung heterogeneity, over 99% of voxels pass the gamma test with the same criteria. Additionally, over 99% of voxels at the bone and lung interfaces pass the gamma test using the 3%/3mm criteria. The main criteria recommended by Low *et al.* for IMRT and VMAT treatment methods is 3%/3mm [38]. The AAPM Task Group (TG-119) also considers 3%/3 mm as an acceptable criterion for the gamma passing rate [39]. Furthermore, the AAPM Task Group (TG-119) suggests a pass rate of more than 95% at the evaluated point when using the criteria of 3%/3mm [39, 40]. Therefore, the model accurately predicts the dose distribution for most voxels in bone, lung, and heterogeneous interfaces by utilizing inputs such as the dose distribution in homogeneous water phantoms and other physical parameters of the heterogeneous phantoms.

The following works can be mentioned as research in the field of dose prediction using deep learning. Nguyen *et al*. used 88 clinical coplanar IMRT prostate patients to predict the dose distribution using u-net architecture [42]. Similarly, Kearney *et al*. designed the architecture of DoseNet and used 51 prostate cancer patients as inputs [43]. Both studies showed that deep learning methods can accurately predict dose distribution utilizing prostate patient's contours. More challenging in dose prediction using the deep learning method is the loss of spatial consistency concerning neighboring anatomy. The results demonstrate the model's ability to predict dose distribution in heterogeneous phantoms with an accuracy comparable to that of the Monte Carlo method, even with significant differences in CT numbers and steep tissue heterogeneity gradients without relying on patient contours.

CONCLUSION

The developed model using the U-net architecture could accurately predict dose distribution in heterogeneous phantoms using inputs such as dose in a homogeneous water phantom and the physical properties of heterogeneous phantoms at a higher speed than Monte Carlo methods.

[DOI: 10.61186/ijrr.24.2.29]

ACKNOWLEDGMENTS

We express appreciation to all colleagues who participated in this research for their time and willingness to share their experiences.

***Conflict of interests*:** Every author declares that they have no competing interests.

***Funding*:** The Amir Kabir University of Technology provided funding for this investigation.

***Authors' contribution*:** M.S.Z. designed the study and served as the corresponding author. N.M. and S.S. developed the model and analyzed the data. H.A.N. assisted in interpreting the results. N.M. wrote the manuscript with guidance from H.A.N. All authors participated in result discussions and contributed to the final manuscript.

REFERENCES

1. Mukai Y, Matsuyama R, Koike I, Kumamoto T, Kaizu H, Homma Y, *et al.* (2019) Outcome of postoperative radiation therapy for cholangiocarcinoma and analysis of dose-volume histogram of remnant liver. *Int J Radiat Oncol,* ***105****(1): e16673.*
2. Kim YL, Suh TS, Choe BY, Choi BO, Chung JB, Lee JW, *et al.* (2016) Dose distribution evaluation of various dose calculation algorithms in inhomogeneous media. *Int J Radiat Res,* ***14****(4): 269-78.*
3. Kim DW, Park K, Kim H, Kim J (2020) History of the photon beam dose calculation algorithm in radiation treatment planning system. *Prog Med Phys,* ***31****(3): 54-2.*
4. Lu L (2013) Dose calculation algorithms in external beam photon radiation therapy. *Int J Cancer Ther Oncol,* ***1****(2): 01025.*
5. Zabihzadeh M, Ghahremani Z, Hoseini SM, Shahbazian H, Hoseini Ghahfarokhi M (2020) Effect of lung inhomogeneity on dose distribution during radiotherapy of patient with lung cancer. *Int J Radiat Res,* ***18****(3): 579-86.*
6. Yang P, Chen Z, Lei Q, Yin C, Zhang S, Wu Z, *et al.* (2021) A new algorithm for dose calculation in heterogeneous lung phantoms under condition of small field size. *Int J Radiat Res,* ***19****(2):259–67.*
7. Zeinali A, Mahani L, Kargar N (2021) Evaluation of full scatter convolution algorithm performance in the presence of inhomogeneities using a novel method of three-dimensional film dosimetry. *Int J Radiat Res,* ***9****(2):391-9.*
8. Sievinen J, Ulmer W, Kaissl W (2005) AAA photon dose calculation model in Eclipse. *Palo Alto Varian Med Syst,* ***118****: 2894.*
9. Ma CM, Li JS, Pawlicki T, Jiang SB, Deng J, Lee MC, *et al.* (2002) A Monte Carlo dose calculation tool for radiotherapy treatment planning. *Phys Med Biol,* ***47****(10): 1671–89.*
10. Bush K, Gagne IM, Zavgorodni S, Ansbacher W, Beckham W (2011) Dosimetric validation of Acuros® XB with Monte Carlo methods for photon dose calculations. *Med Phys,* ***38****(4): 2208-21.*
11. Sarin B, Bindhu B, Saju B, Raghukumar P, Nair RK (2022) Clinical implementation of a PRIMO Monte Carlo-based dose verification and quality assurance model for stereotactic body radiotherapy (SBRT) treatment plans of the lung. *Int J Radiat Res,* ***20****(3): 563-70.*
12. Kang SW, Chung JB, Lee JW, Kim MJ, Kim YL, Kim JS, *et al.* (2017) Dosimetric accuracy of the Acuros XB and Anisotropic analytical algorithm near interface of the different density media for the small fields of a 6-MV flattening-filter-free beam. *Int J Radiat Res,* ***15****(2): 157-65.*
13. Bengio Y, Courville A, Vincent P (2013) Representation learning: A review and new perspectives. *IEEE Trans Pattern Anal Mach Intell,* ***35****(8): 1798-828.*
14. Schmidhuber J (2015) Deep Learning in neural networks: An overview. Vol. 61, Neural Networks. *Neural networks,* ***61****: 85-117.*
15. Chen L, Dong S, Chen Y, Tian L, He C, Tao S (2024) Diagnostic value of chest computed tomography scan based on artificial intelligence and deep learning in children with lobar pneumonia and analysis of image features before and after treatment: A retrospective cohort study. Int J Radiat Res, ***22****(1): 199-205.*
16. Willems S, Crijns W, Sterpin E, Haustermans K, Maes F. (2019) Feasibility of CT-only 3D dose prediction for VMAT prostate plans using deep learning. In Cham: *Springer International Publishing :10–7.*
17. Jiang D, Li T, Mao R, Du C, Liu Y, Liu S, et al. (2019) One-dimensional convolutional network for dosimetry evaluation at organs-at-risk in esophageal radiation treatment planning. In: Artificial Intelligence in Radiation Therapy. *Cham: Springer International Publishing: 86-93.*
18. Barragán-Montero AM, Nguyen D, Lu W, Lin MH, Norouzi-Kandalan R, Geets X, et al. (2019) Three-dimensional dose prediction for lung IMRT patients with deep neural networks: robust learning from heterogeneous beam configurations. *Med Phys,* ***46*** *(8):3679–91.*
19. Shiraishi S and Moore KL (2016) Knowledge-based prediction of three-dimensional dose distributions for external beam radiotherapy. *Med Phys,* ***43****(1): 378-87.*
20. Walters B, Kawrakow I, Rogers DWO (2005) DOSXYZnrc Users Manual. Source. *Nrc Report Pirs,* ***794****: 57-58.*
21. Wu B, Ricchetti F, Sanguineti G, Kazhdan M, Simari P, Chuang M, *et al.* (2009) Patient geometry-driven information retrieval for IMRT treatment plan quality control. *Med Phys,* ***36****(12): 5497-505.*
22. Tran A, Woods K, Nguyen D, Yu VY, Niu T, Cao M, *et al.* (2017) Predicting liver SBRT eligibility and plan quality for VMAT and 4П plans. *Radiat Oncol,* ***12****(1)*: 70-9.
23. Wu B, Pang D, Simari P, Taylor R, Sanguineti G, McNutt T (2013) Using overlap volume histogram and IMRT plan data to guide and automate VMAT planning: A head-and-neck case study. *Med Phys,* ***40****(2): 021714.*
24. Zhu X, Ge Y, Li T, Thongphiew D, Yin FF, Wu QJ (2011) A planning quality evaluation tool for prostate adaptive IMRT based on machine learning. *Med Phys,* ***38****(2): 719-26.*
25. Ronneberger O, Fischer P, Brox T. (2015) U-net: Convolutional networks for biomedical image segmentation. In: International Conference on Medical image computing and computer-assisted intervention. *Cham, Springer international publishing:* ***234****:241.*
26. Çiçek Ö, Abdulkadir A, Lienkamp SS, Brox T, Ronneberger O (2016) 3D U-Net: learning dense volumetric segmentation from sparse annotation. In: International conference on medical image computing and computer-assisted intervention. *Athens, Greece: Springer, 2016. p. 424-32.*
27. Salakhutdinov R HG. (2012) An efficient learning procedure for deep Boltzmann machines. *Neural Comput,* ***24****(8):1967-2006.*
28. Srivastava N, Hinton G, Krizhevsky A, Sutskever I, Salakhutdinov R. Dropout: a simple way to prevent neural networks from overfitting. J Mach Learn Res. 2014;15(1):1929–58.
29. Mohan R, Chui C, Lidofsky L (1986) Differential pencil beam dose computation model for photons. M*ed Phys,* ***13****(1): 64-73.*
30. Papanikolaou N, Battista JJ, Boyer AL, Kappas C, Klein E, Mackie TR, *et al.* (2004) Tissue inhomogeneity corrections for megavoltage photon beams. *AAPM Task Gr,* ***65****: 1-142.*
31. Battista J, Chen J, Sawchuk S, Hajdok G. (2023) Evolution of 3d x-ray dose computation algorithms. *J Phys Conf Ser,* ***2630*** *(1):012008.*
32. Erickson BJ, Korfiatis P, Akkus Z, Kline T, Philbrick K. (2017) Toolkits and libraries for deep learning. *J Digit Imaging,* ***30****(4):400-5.*
33. Carneiro T, Da Nóbrega RV, Nepomuceno T, Bian GB, De Albuquerque VH RFP. (2018) Performance analysis of google colaboratory as a tool for accelerating deep learning applications. *Ieee Access,* ***6****:61677-85.*
34. Kanani P and Padole M (2019) Deep learning to detect skin cancer using google colab. *Int J Eng Adv Technol,* ***8****(6): 2176–83.*
35. Kingma DP, Ba JL. Adam (2015) A method for stochastic optimization. In: 3rd International Conference on Learning Representations, ICLR 2015 - Conference Track Proceedings. *San Diego, CA, USA; 2015. p. 1-15.*
36. Santos CF, Papa JP. (2022) Avoiding overfitting: A survey on regularization methods for convolutional neural networks. *ACM Comput Surv,* ***54****(10):1–25.*
37. Prechelt L. .(1998)Automatic early stopping using cross validation: quantifying the criteria. *Neural networks,* ***11****(4):761–7.*
38. Low DA, Harms WB, Mutic S, Purdy JA. (1998) A technique for the quantitative evaluation of dose distributions. *Medical physics,* ***25*** *(5):656-61.*
39. Ezzell GA, Burmeister JW, Dogan N, Losasso TJ, Mechalakos JG, Mihailidis D, *et al.* (2009) IMRT commissioning: Multiple institution planning and dosimetry comparisons, a report from AAPM Task Group 119. *Med Phys,* ***36****(11): 5359-73.*
40. Low DA, Moran JM, Dempsey JF, Dong L, Oldham M (2011) Dosimetry tools and techniques for IMRT. *Med Phys,* ***38****(3): 1313-38.*
41. Fraass B, Doppke K, Hunt M, Kutcher G, Starkschall G, Stern R VDJ. (1998) American Association of Physicists in Medicine Radiation Therapy Committee Task Group 53: quality assurance for clinical

[DOI: 10.61186/ijrr.24.2.29]

radiotherapy treatment planning. *Med Phys,* ***25****(10):1773–829.*
42. Nguyen D, Long T, Jia X, Lu W, Gu X, Iqbal Z, *et al.* (2019) A feasibility study for predicting optimal radiation therapy dose distributions of prostate cancer patients from patient anatomy using deep learning. *Sci Rep,* ***9****(1): 1076–86.*
43. Kearney V, Chan JW, Haaf S, Descovich M, Solberg TD (2018) DoseNet: A volumetric dose prediction algorithm using 3D fully-convolutional neural networks. *Phys Med Biol,* ***63****(23): 235022.*

[DOI: 10.61186/ijrr.24.2.29]